INTERNATIONAL JOURNAL FOR NUMERICAL METHODS IN FLUIDS, VOL. 19, 1115–1135 (1994)

SIMULTANEOUS SOLUTION OF THE NAVIER–STOKES AND ELASTIC MEMBRANE EQUATIONS BY A FINITE ELEMENT METHOD

MARK PETER RAST*

Department of Applied Mathematical Studies, University of Leeds, Leeds LS2 9JT, U.K.

SUMMARY

Fluid flow through a significantly compressed elastic tube occurs in a variety of physiological situations. Laboratory experiments investigating such flows through finite lengths of tube mounted between rigid supports have demonstrated that the system is one of great dynamical complexity, displaying a rich variety of self-excited oscillations. The physical mechanisms responsible for the onset of such oscillations are not yet fully understood, but simplified models indicate that energy loss by flow separation, variation in longitudinal wall tension and propagation of fluid elastic pressure waves may all be important. Direct numerical solution of the highly non-linear equations governing even the most simplified two-dimensional models aimed at capturing these basic features requires that both the flow field and the domain shape be determined as part of the solution, since neither is known *a priori*. To accomplish this, previous algorithms have decoupled the solid and fluid mechanics, solving for each separately and converging iteratively on a solution which satisfies both. This paper describes a finite element technique which solves the incompressible Navier–Stokes equations simultaneously with the elastic membrane equations on the flexible boundary. The elastic boundary position is parametized in terms of distances along spines in a manner similar to that which has been used successfully in studies of viscous free surface flows, but here the membrane curvature equation rather than the kinematic boundary condition of vanishing normal velocity is used to determine these distances and the membrane tension varies with the shear stresses exerted on it by the fluid motions. Both the grid and the spine positions adjust in response to membrane deformation, and the coupled fluid and elastic equations are solved by a Newton–Raphson scheme which displays quadratic convergence down to low membrane tensions and extreme states of collapse. Solutions to the steady problem are discussed, along with an indication of how the time-dependent problem might be approached.

KEY WORDS Collapsible tube flow Moving boundary problems Adaptive finite element spine method Physiological flows

1. INTRODUCTION

The partial collapse of an elastic tube conveying fluid under sufficiently low transmural pressure (the difference between internal and external pressures) occurs in a variety of physiological settings. These include veins above the level of the heart, due to the reduction in hydrostatic pressure with height; abdominal veins just before they enter the chest, due to the abdominal–thoracic pressure contrast; veins in the legs during muscle contraction; intramyocardial coronary blood vessels during systole; pulmonary blood vessels in the upper portions of the lung; arteries compressed by a blood pressure cuff or within the chest during cardiopulmonary resuscitation; large airways during forced expiration;

* Present address: Advanced Study Program, National Center for Atmospheric Research, PO Box 3000, Boulder, CO 80307-3000, U.S.A. NCAR is sponsored by the National Science Foundation.

CCC 0271–2091/94/241115–21

Received 8 March 1994
Revised 2 September 1994

the ureter during peristaltic pumping; and others.[1–4] Interest in such flows stems not only from the intriguing mix of solid and fluid mechanics which governs their behaviour, but also from the possibility that fluid dynamical factors may play a role in human disease. Regions of low arterial wall shear stress appear to be those most subject to atherosclerosis.[2,5,6] Additionally, wheezing,[3,7,8] the Korotkoff sounds heard during blood pressure measurement,[2–4,9,10] flow oscillations in the cerebral cortex,[11] and vena cava 'chatter' during bypass surgery[4,12] may all be examples of self-excited flow-induced oscillations in partially collapsed tubes. The understanding of such oscillations may thus have clinical significance.

Over the past years many laboratory experiments have been conducted to investigate the properties of fluid flow through partially collapsed tubes. Typically, a section of compliant tubing is mounted horizontally between two rigid tubes and sealed within a chamber, a configuration called a Starling resistor.[13,14] The longitudinal tension, external pressure, flow rate and upstream and downstream pressures can then all be varied. Differing results more or less applicable to various physiological systems[3] are obtained, but some effects are common to all investigations. These include flow rate limitation, in which the maximum flow rate does not increase with a decrease in downstream pressure, and self-excited oscillations, in which the tube undergoes large-amplitude variations in cross-sectional area and outflow rate.[9,15–23] Such oscillations occur over a wide range of parameter values and despite significant theoretical efforts remain incompletely understood. No single physical cause appears responsible for all the apparent oscillation types, which range from periodic oscillations of rather low frequency to aperiodic, possibly chaotic, high-frequency fluctuations.[21,23,24]

Until recently, theoretical elastic tube models were predominantly of two basic types: one-dimensional models in which flow variables are integrated over the tube cross-section with a simple elastic 'tube law' relating the cross-sectional area to the transmural pressure,[2,25,26] and lumped-parameter models in which flow variables are also integrated along the tube, the geometry of the collapsible section is represented by a single time-dependent variable such as the tube's minimum cross-sectional area, and the elastic properties of the tube are reduced to a relationship between the transmural pressure and the cross-sectional area at the point of maximum collapse.[2,15,16,27–29] Both types of model have been successful at predicting the occurrence of self-excited oscillations. Additionally, the lumped parameter models have emphasized the importance of external constraints imposed by rigid supports and have demonstrated the sensitivity of oscillatory instabilities to the amount of energy dissipated downstream of the constriction.[29] Unfortunately, lumped-parameter models exclude the possibility of fluid-elastic pressure waves and therefore, not distinguishing between super- and subcritical flows, excluding choking. One-dimensional models, on the other hand and in agreement with experiment (see e.g. References 17 and 18), predict no steady flow if the fluid velocity anywhere matches or exceeds the propagation speed of small-amplitude pressure waves. Such models have also identified the phenomenon of flow limitation with supercritical flow speeds and the accompanying insensitivity to downstream pressure changes[30] and have demonstrated that elastic jumps, analogous to shocks in compressible fluids and hydraulic jumps in free surface flows, can occur in compliant tubes.[25,31–33] (The propagation of elastic jumps has been proposed as an alternative mechanism for the production of Korotkoff sounds[34–36] and as an explanation for the 'pistol shot' sounds produced by leaky heart valves.[33]) However, such one-dimensional models in their simplest form are local in character. They may be able to predict the onset of oscillations based on local stability criteria, but they cannot model subsequent development of the instability. Additionally, experiments indicate that non-local effects may be important even at the onset. To overcome these drawbacks, recent work has emphasized hybrid models which combine the one-dimensional approach with important aspects of the lumped-parameter models. Such hybrid models have included the effects of rigid upstream and downstream mounts, longitudinal tension in the elastic section[37–40] and energy loss by intermittent flow separation downstream of the point of maximum collapse.[37,39,40] They confirm

that oscillations occur if the flow becomes supercritical anywhere in the elastic tube. A primary instability mechanism appears to be associated with the movement of the flow separation point in response to pressure waves propagating along the tube. The precise degree of energy loss in the separated flow is a critical factor in the instability and one that is parametized in a highly simplified manner in these models.

Recently a very different mechanism has been proposed to account for the breakdown of steady flow in a collapsible tube[41] and it is the investigation of this mechanism, in addition to the desire to study more complete fluid dynamic and solid mechanic formulations than the above simplified models allow, that has prompted numerical solution of the full Navier–Stokes and elastic membrane equations. The proposal relies on the fact that viscous shear stresses exerted by the fluid cause the longitudinal tension in the tube wall to decrease with distance downstream. For a given upstream value the tension may fall to zero at some point along the tube if the tube is long enough. Such a state of zero tension presumably results in extreme wall flexibility and unsteady motions. Initial study of low-Reynolds-number flow through a two-dimensional channel with collapsible walls utilizing lubrication theory found that when the downstream tension became very low, major deformation of the wall occurred, resulting in large wall slopes and violation of the initial assumptions of the model.[41] The lubrication approximation was therefore subsequently abandoned and studies of both zero-[42] and non-zero-[43] Reynolds-number flows through a two-dimensional channel with a single elastic wall segment have begun. This simplified geometry was chosen not only for computational ease but also because previous experimental[44,45] and numerical[46,47] work indicates that channel flows subject to time-dependent asymmetric deformations give rise to vorticity waves not seen with symmetric deformation. It should be noted that other authors have considered coupled fluid elastic problems in a variety of applications (see e.g. References 48–63), some of which were two-dimensional elastic tube or channel studies supporting a number of the conclusions drawn from the one-dimensional and hybrid models discussed above,[7,50–52] but all have involved simplifications of the problem's elastic or hydrodynamic properties. We pursue such studies here without linearization of the fluid motions or restriction to small-amplitude boundary deformation and solve the fully non-linear Navier–Stokes and elastic membrane equations, albeit in the highly simplified geometry mentioned above and to be described in more detail in the next section.

2. FORMULATION

We consider the steady flow of an incompressible Newtonian fluid through a two-dimensional channel with an elastic wall which can suffer large-amplitude deformations. The geometry considered is shown in Figure 1. One segment of an otherwise rigid channel is replaced by a thin-walled membrane under longitudinal tension. The tension is held fixed at a specified value T_0 at the right-hand attachment point, but otherwise varies owing to stresses exerted upon it by the fluid flow. The inflow is specified to be plane Poiseuille with flow rate Q, while the outflow is specified to be both parallel and stress-free. A long enough channel is generally employed so that the flow is fully developed before exiting the downstream end of the flow domain. No-slip and impermeable boundary conditions are applied on the side walls (including the elastic section), forcing both components of the velocity to vanish there. The pressure in the fluid is scaled by specifying P_0 at the lower exit point to be identically zero, and an external pressure P_e is applied.

Flow in such a geometry can be described by the two-dimensional Navier–Stokes equations, with the elastic properties of the boundary being modelled by simple force balance across a thin inertialess wall. The resulting coupled set of equations may be expressed non-dimensionally by taking u_0 as the characteristic velocity and H as the unit of distance. There are then at least two possible pairs of scalings for the pressure and tension: a dynamic scaling, $\rho_0 u_0^2$ for pressure and $\rho_0 u_0^2 H$ for tension, or a viscous scaling, $\mu u_0/H$ for pressure and μu_0 for tension, where ρ_0 is the fluid density and μ is the

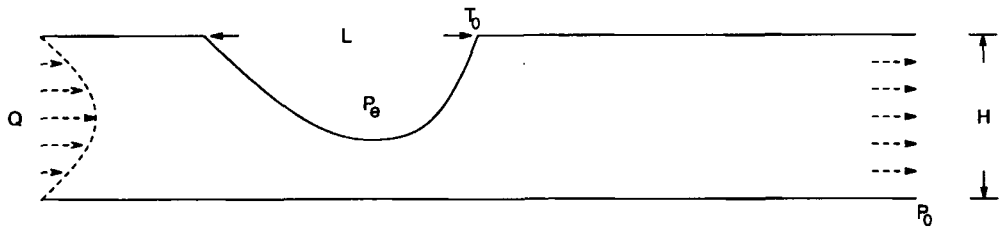

Figure 1. Domain geometry. Two-dimensional channel with an elastic wall section of length L and undeformed height H. Membrane tension specified as T_0 at the right attachment point. Pressure scaled to equal P_0 at the lower exit point, with an external pressure P_e applied. Incoming flow is plane Poiseuille with flow rate Q; outflow is parallel and stress-free

dynamic viscosity. We choose the first of these scalings so that viscosity enters the equations of motion only through the Reynolds number $Re = \rho_0 u_0 H/\mu$. With this non-dimensionalization the steady incompressible Navier–Stokes equations become

$$\frac{\partial u_k}{\partial x_k} = 0, \tag{1}$$

$$u_k \frac{\partial u_j}{\partial x_k} + \frac{\partial P}{\partial x_j} - \frac{1}{Re}\frac{\partial^2 u_j}{\partial x_k \partial x_k} = 0 \tag{2}$$

for the velocity components u_j and pressure P, while the elastic membrane equations can be written as

$$P - P_e = -\kappa T, \tag{3}$$

$$\frac{dT}{ds} = -\frac{1}{Re}\hat{n} \cdot \nabla(\mathbf{u} \cdot \hat{t}), \tag{4}$$

where T is the membrane tension, κ is the membrane curvature and $\hat{n}$ and $\hat{t}$ are the unit normal and tangential vectors respectively. Equation (3) relates the total normal stress on the membrane which results from the transmural pressure to the normal force exerted by the tension. The curvature by which the tension generates this force may be expressed as the derivative of the tangent angle to the elastic boundary along the membrane:

$$\kappa = \frac{d\phi}{ds}. \tag{5}$$

The relationship between the tension in the membrane and the tangential shear stresses exerted on it by fluid motions is expressed by equation (4). The sign is chosen such that $\hat{n}$ is the outward normal and $\hat{t}$ points in the direction of increasing arc length s (the downstream direction for the undeformed membrane). We solve equations (1)–(4) by finite element techniques in primitive fluid variables u, v and P, with two additional unknowns, membrane tension and height, active on the elastic boundary.

3. COMPUTATION

Previous numerical work on this problem[42,43] has employed an iterative scheme which decouples the solution of the fluid equations from that of the membrane equations. Briefly, such a scheme proceeds as follows. An initial membrane shape is assumed and equations (1) and (2) or their zero-Reynolds-number equivalents are solved in this specified geometry. The stresses exerted on the membrane are then calculated and equation (3) is used to update the membrane position. The process is repeated until

a solution is found which satisfies both the fluid and solid mechanics. Such a method is similar to iterative techniques used in early computations of viscous free surface flows.[64–68] In such flows the normal velocity and tangential shear stress must vanish and normal stresses must balance the product of surface tension and curvature at the free surface. The iterative schemes devised relax one of these boundary conditions, usually either the kinematic normal velocity (see e.g. References 64 and 67) or the normal stress balance (see e.g. References 65 and 67) condition, when solving the fluid equations and then use it subsequently to update the location of the free surface. The best choice of boundary condition to relax in the free surface problem depends on the surface tension of the fluid.[65,67] For high surface tensions relaxation of the normal stress condition proves best, while for low tensions kinematic iteration proves more useful.[67] At intermediate tensions both schemes converge poorly, often only with some underrelaxation. The elastic membrane problem is similar, except that both components of the velocity vanish and the tension can vary with position on the boundary. The previously described elastic membrane iterative scheme[42,43] employs the normal stress balance condition to determine the boundary position and fails at low values of the membrane tension just as the comparable scheme does for free surface flows. This has prompted the current research into an alternative solution technique which can yield results over a wide range of membrane tensions and hopefully contribute to an understanding of the physical rather than numerical mechanisms behind the breakdown of steady flow in this system. The technique described in this paper again relies on experience gained by researchers of viscous free surface flows.[69–77] It determines the position and tension of the elastic boundary and the interior pressure and fluid velocity fields by solving equations (1)–(4) simultaneously using finite element techniques and spines to parametrize the elastic boundary location. For completeness we summarize the entire method in this section, but claim originality only in how the geometry of this particular problem is approached, how variable tension is incorporated and how the membrane curvature equation is used to directly determine the boundary position.

Many other numerical methods have been devised to study problems with moving boundaries. These include, but are not limited to, the finite difference arbitrary Lagrangian–Eulerian[78–81] and closely related deformable cell[82] methods as well as the marker-and-cell[83–85] and related volume-of-fluid[86] methods and boundary element methods.[87–89] To a lesser extent the arbitrary Lagrangian–Eulerian scheme has been used in conjunction with finite element discretization.[90] Additionally, global mapping of an irregular and changing flow domain to a rectangular space[91–93] on which standard finite difference discretization can be applied has also been used successfully (see e.g. References 94 and 95), as have more exotic approaches such as expressing the moving boundary in terms of a localized force distribution.[96,97] Space does not permit review of each of these methods in detail, but we have chosen an adaptive finite element method based on its straight-forward applicability to problems involving non-linear flows of moderate Reynolds number in irregularly shaped domains. Adaptation of the grid to the boundary shape, as determined by the solution of the problem, will turn out to be particularly advantageous, since the grid distortion is not confined to the boundary elements but is distributed through the domain. The remainder of this section details how we proceed.

We begin by dividing the flow domain into six-node triangular finite element subdomains. The shapes and locations of these subdomains are linked to the position of the elastic boundary. This is accomplished by constructing the grid so that elemental nodes under the elastic section lie along radial spines which emanate from an origin whose position is in turn determined by the central membrane height. Each spine k is defined by the Cartesian co-ordinates of its base point, x_b^k and y_b^k, and the direction from that point to the origin or equivalently the angle which the spine makes with the vertical, θ^k. The extensions of a number of these spines towards their origin outside the flow domain are shown with dashed lines in Figure 2, while the corresponding base points are marked with boxes. Also evident in this figure is the substantial change in the grid structure under the collapsible section which results from membrane deformation. One significant advantage of such grid adjustment is that the grid

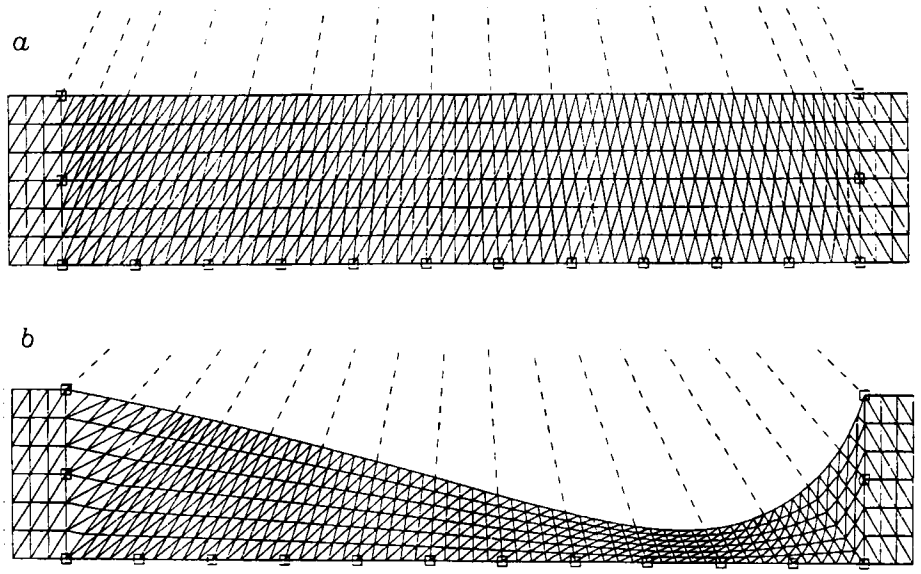

Figure 2. Computational grid beneath the elastic section (*a*) before and (*b*) after membrane deformation. Boxes indicate the location of some representative spine bases; dashed extensions above the domain point towards the spine origin. The thickened element in (*b*) is that shown in detail in Figure 3. Note that the actual computations were done with much higher resolution, as indicated in Section 4 of the text.

is not overtaken by the boundary. Instead, the position of node i on spine k is given in terms of a fixed fraction w_i^k of the spine height h^k as

$$x_i^k = x_b^k + w_i^k h^k \sin\theta^k, \tag{6a}$$

$$y_i^k = y_b^k + w_i^k h^k \cos\theta^k, \tag{6b}$$

where the spine height is simply the distance from the spine base to the elastic surface in the direction of the origin and is an unknown in the problem. All computations for this paper were done with a single origin, but generalization to multiple origins makes it possible to avoid singular grids even in the case of a very highly distorted and folded boundary. Additional refinement of the grid can be accomplished by manual adjustment of the spine origin position or by grid stretching. In these calculations we made provision for independent stretching in the horizontal and vertical directions but implemented only horizontal stretching downstream of the collapsible portion. This allowed increased resolution by finer grid spacing in the region of rapid flow expansion and simultaneous coarsening further downstream where the flow was nearly fully developed and less resolution was required. It also facilitated a smoother transition in finite element size from the distorted grid under the elastic section to the regular one downstream.

Individual elements of the grid are mapped from global Cartesian (x, y) co-ordinates to local (ζ, η) co-ordinates as shown in Figure 3. The mapping here is done on local subdomains rather than globally as in a boundary-fitted global mapping scheme but is otherwise very similar, since the shape of the local subdomain depends on the elastic boundary position as does of course the domain shape in a global mapping scheme. The variables u, v, P and T are expanded isoparametrically (same representation for co-ordinates as variables) in area co-ordinates,[98,99] employing a mixed interpolation (see e.g.

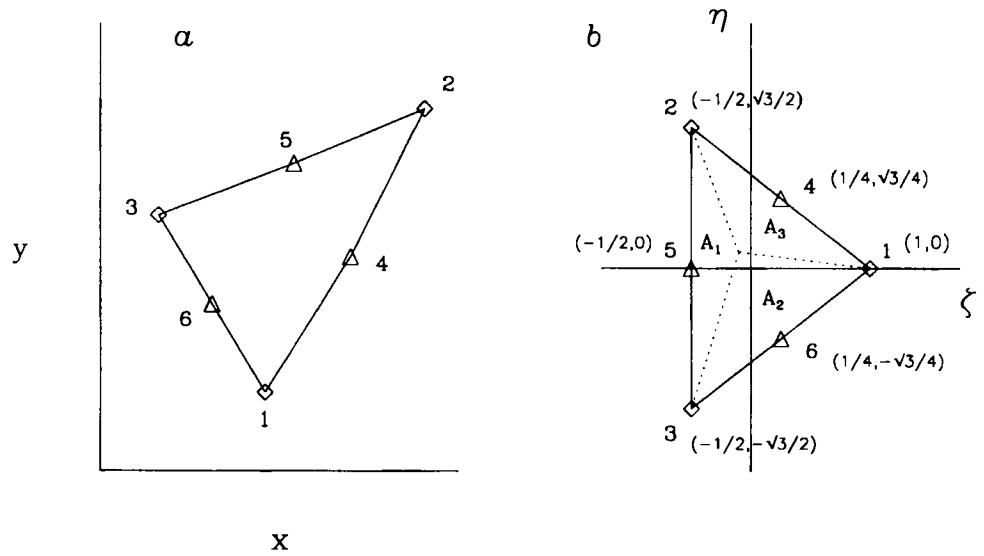

Figure 3. Mapping between global (x, y) and local (ζ, η) co-ordinates. Nodes 1–3 are velocity and pressure nodes, while nodes 4–6 are velocity-only nodes. Spine height is an active variable on nodes 3, 5 and 2, and tension on 3 and 2, if the element is positioned such that these nodes lie along the elastic boundary

Reference 100), with u, v, x and y sharing quadratic and P and T linear expansions:

$$u = \sum_{i=1}^{6} u_i N_i(\zeta, \eta), \qquad v = \sum_{i=1}^{6} v_i N_i(\zeta, \eta),$$

$$x = \sum_{i=1}^{6} x_i(h, \theta) N_i(\zeta, \eta), \qquad y = \sum_{i=1}^{6} y_i(h, \theta) N_i(\zeta, \eta), \tag{7}$$

$$P = \sum_{i=1}^{3} P_i L_i(\zeta, \eta), \qquad T = \sum_{i=2}^{3} T_i L_i(\zeta, \eta).$$

Here L_i and N_i are linear and quadratic shape functions respectively, with $L_i = A_i/A$ ($A = A_1 + A_2 + A_3$; Figure 3) and

$$\begin{aligned} N_1 &= L_1(2L_1 - 1), \qquad N_2 = L_2(2L_2 - 1), \qquad N_3 = L_3(2L_3 - 1), \\ N_4 &= 4L_1L_2, \qquad N_5 = 4L_2L_3, \qquad N_6 = 4L_1L_3. \end{aligned} \tag{8}$$

Such shape functions are taken to be non-zero only within each individual element. Additionally, they have the properties that at any point within an element

$$\sum_{i=1}^{6} N_i(\zeta, \eta) = \sum_{i=1}^{3} L_i(\zeta, \eta) = 1 \tag{9a}$$

and at any node i

$$L_j(x_i) = \delta_{ij}, \qquad N_j(x_i) = \delta_{ij}. \tag{9b}$$

Thus nodal velocities are defined at all six nodes of each element while pressure is an active variable only at nodes 1–3 (Figure 3). Velocities vary quadratically while pressure varies linearly between

nodes. Along the elastic boundary, only those shape functions associated with nodes which lie on it are non-zero and the elements have been oriented so that these always number 3, 5 and 2. Tension is an active variable at two of these (nodes 3 and 2) while membrane height is active at all three. The co-ordinates x and y of all nodes below the elastic boundary depend on both the boundary and spine origin positions and thus so too does the Jacobian of co-ordinate transformation $\mathbf{J}_0$ and its determinant for those elements which contain these nodes. Explicitly,

$$\mathbf{J}_0 = \begin{pmatrix} \partial x/\partial\zeta & \partial y/\partial\zeta \\ \partial x/\partial\eta & \partial y/\partial\eta \end{pmatrix}, \tag{10}$$

where $\partial x/\partial\zeta$, $\partial x/\partial\eta$, $\partial y/\partial\zeta$ and $\partial y/\partial\eta$ can all be evaluated from Equations (7) and depend on h and θ through x_i and y_i (Equations (6)).

Equations determining the nodal values of u, v, P, h and T are derived by the Galerkin method of weighted residuals. The Navier–Stokes and elastic membrane equations are multiplied by the finite element basis functions and are integrated over the domain. Values of the variables are found such that these residuals vanish. Weighting the continuity equation (1) with the linear shape functions and integrating yields k algebraic equations, the same number as the number of pressure unknowns:

$$R_c^k = \sum_{i=1}^{6} u_i \int\int L_k \frac{\partial N_i}{\partial x}\,\mathrm{d}x\,\mathrm{d}y + \sum_{i=1}^{6} v_i \int\int L_k \frac{\partial N_i}{\partial y}\,\mathrm{d}x\,\mathrm{d}y = 0. \tag{11}$$

Likewise, weighting the momentum equations (2) with the quadratic shape functions and integrating provides the l equations necessary to determine the nodal velocity values. Explicitly, the x-momentum equation yields

$$\begin{aligned} R_x^l = {} & \sum_{i=1}^{6}\sum_{j=1}^{6} u_i u_j \int\int N_l N_j \frac{\partial N_i}{\partial x}\,\mathrm{d}x\,\mathrm{d}y + \sum_{i=1}^{6}\sum_{j=1}^{6} u_i v_j \int\int N_l N_j \frac{\partial N_i}{\partial y}\,\mathrm{d}x\,\mathrm{d}y \\ & - \sum_{j=1}^{3} P_j \int\int L_j \frac{\partial N_l}{\partial x}\,\mathrm{d}x\,\mathrm{d}y + \sum_{i=1}^{6} u_i \int\int \frac{1}{Re}\frac{\partial N_i}{\partial x}\frac{\partial N_l}{\partial x}\,\mathrm{d}x\,\mathrm{d}y \\ & + \sum_{i=1}^{6} u_i \int\int \frac{1}{Re}\frac{\partial N_i}{\partial y}\frac{\partial N_l}{\partial y}\,\mathrm{d}x\,\mathrm{d}y + \sum_{j=1}^{3} P_j \int N_l L_j (\hat{i}\cdot\hat{n})\mathrm{d}s \\ & - \sum_{i=1}^{6} u_i \int \frac{1}{Re} N_l \frac{\partial N_i}{\partial x}(\hat{i}\cdot\hat{n})\mathrm{d}s - \sum_{i=1}^{6} u_i \int \frac{1}{R_e} N_l \frac{\partial N_i}{\partial y}(\hat{j}\cdot\hat{n})\mathrm{d}s = 0, \end{aligned} \tag{12}$$

with Galerkin weighted residuals R_y^l of similar form stemming from the y-momentum equation. Here the divergence theorem has been applied to reduce derivatives within the integrals to first-order, consistent with the low-order expansions of equations (7). Making the transformations

$$\begin{pmatrix} \partial/\partial x \\ \partial/\partial y \end{pmatrix} = \frac{1}{|\mathbf{J}_0|}\begin{pmatrix} \partial y/\partial\eta & -\partial y/\partial\zeta \\ -\partial x/\partial\eta & \partial x/\partial\zeta \end{pmatrix}\begin{pmatrix} \partial/\partial\zeta \\ \partial/\partial\eta \end{pmatrix} \tag{13a}$$

and

$$\int\int \mathrm{d}x\,\mathrm{d}y = \int\int |\mathbf{J}_0|\,\mathrm{d}\zeta\,\mathrm{d}\eta, \tag{13b}$$

the integrals in equations (11), (12) and R_y^l can be written in terms of the local co-ordinates and evaluated for each element by Gaussian quadrature.[101] Quadrature formulae of the same order as the

polynomial degree of the integrand are employed so that the integrals are evaluated exactly. Only those integrals containing two derivatives of the shape functions depend on the element geometry through the determinant of the co-ordinate transformation Jacobian. These must be evaluated for each element individually, while the remaining integrals have the same values for all elements. Since u and v are known on all boundaries except the outflow, where P and v are specified, the only momentum residual boundary integrals which must be evaluated are those contributing to equation (12) in the elements bordering the outflow. Boundary integrals for the interior elements cancel between neighbours, while on other exterior boundaries R_x^l and R_y^l need not be assembled, since u and v are known.

On the elastic portion of the boundary, membrane height and tension are additional unknowns to be evaluated. Residuals of equations (3) and (4) are orthogonalized with respect to the finite element quadratic and linear basis functions respectively, since spatial co-ordinates and thus h are expanded quadratically while tension is expanded linearly like pressure. Integrated along the elastic boundary, equation (3) thus yields

$$R_e^l = -P_e \int_E N_l \mathrm{d}s + \sum_{j=2}^{3} P_j \int_E N_l L_j \mathrm{d}s + \sum_{j=1}^{3} T_j \int_E N_l L_j \frac{\mathrm{d}\phi}{\mathrm{d}s} \mathrm{d}s = 0. \tag{14a}$$

When then integrated by parts and expressed in terms of local co-ordinates for an individual element, this becomes

$$R_e^l = -P_e \int_0^1 N_l \frac{\mathrm{d}s}{\mathrm{d}L_3} \mathrm{d}L_3 + \sum_{j=2}^{3} P_j \int_0^1 N_l L_j \frac{\mathrm{d}s}{\mathrm{d}L_3} \mathrm{d}L_3 - \sum_{j=2}^{3} T_j \int_0^1 \phi L_j \frac{\mathrm{d}N_l}{\mathrm{d}L_3} \mathrm{d}L_3$$
$$- \sum_{j=2}^{3} T_j \int_0^1 \phi N_l \frac{\mathrm{d}L_j}{\mathrm{d}L_3} \mathrm{d}L_3 + T_1\phi_1 - T_0\phi_0 = 0, \tag{14b}$$

where ϕ and $\mathrm{d}s/\mathrm{d}L_3$ can be expressed as

$$\phi = \tan^{-1}\left(-\frac{\mathrm{d}y/\mathrm{d}L_3}{\mathrm{d}x/\mathrm{d}L_3}\right), \tag{15}$$

$$\frac{\mathrm{d}s}{\mathrm{d}L_3} = \sqrt{\left[\left(\frac{\mathrm{d}x}{\mathrm{d}L_3}\right)^2 + \left(\frac{\mathrm{d}y}{\mathrm{d}L_3}\right)^2\right]}.$$

The derivatives $\mathrm{d}x/\mathrm{d}L_3$ and $\mathrm{d}y/\mathrm{d}L_3$ can be easily evaluated in terms of nodal co-ordinates using the isoparametric expansions given by (7). The endpoint terms $T_1\phi_1$ and $T_0\phi_0$ make a net contribution only in those two elements containing either the first or the last node of the elastic membrane. Note that both ϕ and $\mathrm{d}s/\mathrm{d}L_3$ are functions of x and y and therefore of spine height h.

From the shear stress equation one can obtain the residual equations which make it possible to determine membrane tension. The unit normal and tangential vectors on the elastic boundary are

$$\hat{n} = \left(\frac{\mathrm{d}y}{\mathrm{d}L_3}\,\hat{\imath} - \frac{\mathrm{d}x}{\mathrm{d}L_3}\,\hat{\jmath}\right) \Big/ \frac{\mathrm{d}s}{\mathrm{d}L_3}, \tag{17a}$$

$$\hat{t} = \left(-\frac{\mathrm{d}x}{\mathrm{d}L_3}\,\hat{\imath} - \frac{\mathrm{d}y}{\mathrm{d}L_3}\,\hat{\jmath}\right) \Big/ \frac{\mathrm{d}s}{\mathrm{d}L_3}. \tag{17b}$$

Substituting these into equation (4) and integrating along the boundary yields

$$R_t^k = \sum_{j=2}^{3} T_j \int_0^1 L_k \frac{dL_j}{dL_3} dL_3 - \sum_{i=1}^{6} u_i \int_0^1 \frac{1}{Re} L_k \frac{dy}{dL_3} \frac{dx/dL_3}{ds/dL_3} \frac{\partial N_i}{\partial x} dL_3$$
$$- \sum_{i=1}^{6} v_i \int_0^1 \frac{1}{Re} L_k \frac{dy}{dL_3} \frac{dy/dL_3}{ds/dL_3} \frac{\partial N_i}{\partial x} dL_3 + \sum_{i=1}^{6} u_i \int_0^1 \frac{1}{Re} L_k \frac{dx}{dL_3} \frac{dx/dL_3}{ds/dL_3} \frac{\partial N_i}{\partial y} dL_3$$
$$+ \sum_{i=1}^{6} v_i \int_0^1 \frac{1}{Re} L_k \frac{dx}{dL_3} \frac{dy/dL_3}{ds/dL_3} \frac{\partial N_i}{\partial y} dL_3 = 0. \tag{18}$$

The partial derivatives with respect to global co-ordinates x and y in this expression can be easily written in terms of local co-ordinates ζ and η using (13a). The integrals in (18) then depend on the spine heights directly through nodal values x_i and y_i as well as indirectly through the determinant of the co-ordinate transformation Jacobian, $|\mathbf{J}_0|$, and ds/dL_3. Such dependences are important in finding a solution which satisfies equations (11), (12), $R_y^l = 0$, (14) and (18) simultaneously.

By the finite element/Galerkin method we have reduced the continuous problem of equations (1)–(4) to a set of discrete non-linear algebraic equations. The non-linearities result from both momentum advection and membrane curvature. For a solution to exist, nodal values of u, v, P, h and T must be found such that residuals R_x^l, R_y^l, R_c^k, R_e^l, and R_t^k vanish simultaneously. This can be done by a Newton–Raphson scheme, solving the linearized equations.

$$\left.\frac{\partial \mathbf{R}}{\partial \boldsymbol{\alpha}}\right|_{\boldsymbol{\alpha}_n} \Delta\boldsymbol{\alpha} \approx -\mathbf{R}(\boldsymbol{\alpha}_n) \tag{19}$$

iteratively. Here $\boldsymbol{\alpha}$ is the vector of nodal unknowns, $\Delta\boldsymbol{\alpha} = \boldsymbol{\alpha}_{n+1} - \boldsymbol{\alpha}_n$, $\mathbf{R}$ is the associated residual vector and n indicates the iteration number. Updated values $\boldsymbol{\alpha}_{n+1}$ are determined from the previous iteration $\boldsymbol{\alpha}_n$, and since the scheme is based on a truncated Taylor series expansion for $\mathbf{R}$, convergence to the solution $\Delta\boldsymbol{\alpha} = 0$ and $\mathbf{R} = 0$ is quadratic as the solution is approached. In our calculations we are able to obtain a solution with max $|\alpha_{n+1}^i - \alpha_n^i| < 10^{-6}$ and max $|R^i(\alpha_n)| < 10^{-6}$ in typically four to six iterations when using zeroth-order continuation from a previously obtained solution. For such continuation to work at all, the parameter changes must of course be small enough so that the new values lie within the domain of convergence of a new solution. The size of this domain is particularly sensitive to errors in the estimation of the membrane position. One of the benefits of the Newton–Raphson scheme is that the Jacobian matrix $\partial\mathbf{R}/\partial\boldsymbol{\alpha}$ contains information on the sensitivity of the solution to changes in parameter values. This information can be used to construct an initial guess from a previous solution (first-order continuation), making larger parameter steps between solutions possible. Additionally, the Jacobian contains information about the stability of a converged solution to small perturbations (see e.g. References 74 and 102), and although not yet studied in detail for this problem, such information may prove very valuable in understanding the physical breakdown of the steady solutions to be identified in Section 4.

The element level structure of equation (19) is illustrated in Figure 4. In general, the top left 15×15 submatrix of the Jacobian array contains non-zero values for all elements in the domain. For elements lying entirely between two rigid boundaries, these are the only non-zero entries. For elements which lie under but do not border the elastic membrane, columns 16–18 of rows 1–15 may also be non-zero, because the shape of these elements is affected by the position of the elastic boundary. Finally, the elements directly neighbouring the flexible boundary are those containing nodes on which the membrane height and tension are active variables, and for these the last five rows of the element level Jacobian can have non-zero entries as well. The global Jacobian matrix $\partial\mathbf{R}/\partial\boldsymbol{\alpha}$, solution

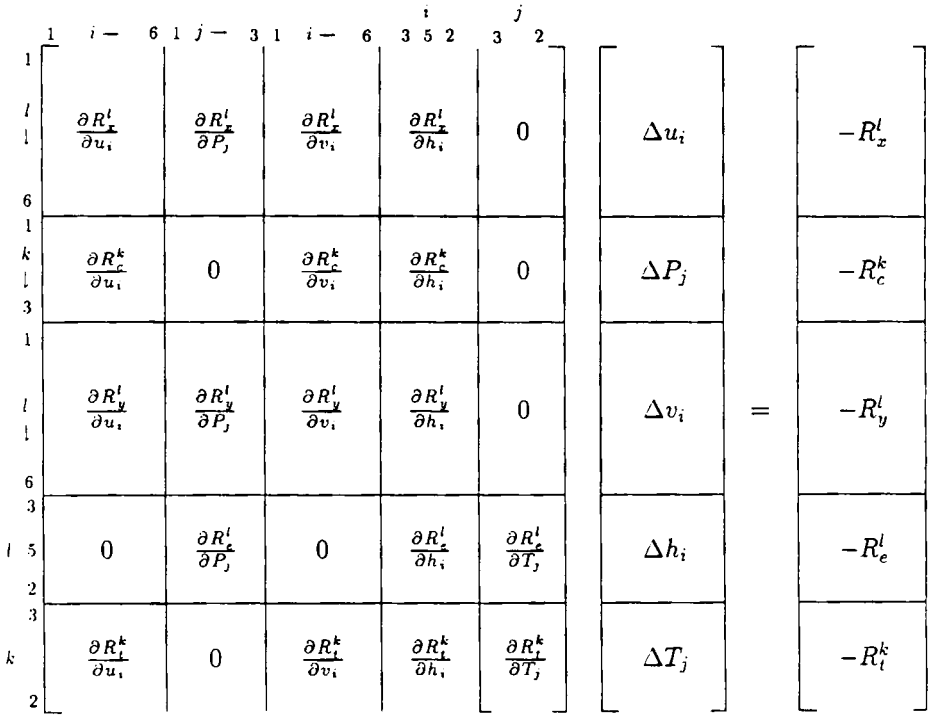

Figure 4. Element level structure of the Jacobian matrix and solution increment and residual vectors. The right-hand five columns and bottom five rows of the Jacobian have non-zero entries only for those elements lying under the elastic membrane or bordering it (see text)

increment $\Delta\boldsymbol{\alpha}$ and residual vector $\mathbf{R}$ are assembled from these element level contributions. We employ a frontal solution technique,[103–106] so the assembly proceeds element-by-element and intermittently. As variables are fully summed (no longer depend on subsequent elements or equations) they are eliminated. This is followed by further assembly and Gaussian elimination, and when complete, the solution is determined by back substitution. Such an algorithm is useful in minimizing memory requirements and imposes no stringent constraints on node numbering. This is particularly important in moving boundary problems, since the spine orientations are unrestricted by nodal requirements and can be adapted freely to the domain geometry.[73] The front width and thus memory storage requirements of this technique does depend on the element numbering, and to keep this as small as possible, the elements are numbered sequentially along the shortest dimension of the domain.

To successfully implement the Newton–Raphson scheme outlined above, one must of course compute the Jacobian matrix correctly. Derivatives with respect to spine heights are difficult to evaluate if the residuals are expressed in global co-ordinates, since then both the integrand and the limits of integration depend on the spine height, but when evaluated in the local computational domain, this difficulty vanishes.[71,73] In the isoparametrically transformed co-ordinates the element shapes are fixed and the limits of integration constant. It then remains important only to correctly identify all the spine height dependences, including those hidden in the determinant $|\mathbf{J}_0|$, as identified above. Also note that if the position of the spine origin is allowed to adjust in response to membrane deformation, then θ_k for all spines depends on the membrane position. A convenient way of defining this dependence is to express the origin position in terms of a particular spine height, e.g. the mid-membrane height h_{mid}. Then additional derivatives with respect to h_{mid} may be readily evaluated for all elements under the moving boundary and incorporated into the Newton–Raphson scheme. Alternatively, the origin

position may be held fixed during the iteration process and updated with the initial guess before continuation to a new solution.

4. RESULTS

Table I lists the properties of some solutions determined as above and displayed in Figures 5–9. The control parameters Re, P_e and T_0 have been defined previously (see Section 2), $P_t = P - P_e$ is the transmural pressure across the upper boundary immediately before the collapsible section of the channel, and the remaining tabulated quantities are the extrema of the field variables: membrane height y, horizontal velocity u, vertical velocity v, pressure P and membrane tension $\Delta T = T - T_0$. All solutions are for a channel with dimensions of 5 units before, 5 units under and 20 units after the elastic section and for an inflow rate Q of unity. A computational grid of 5192 elements was used. These were distributed as in Figure 2, with 22 spanning the vertical dimension in the undeformed portion and subtotals of 990 before, 1452 under and 2750 after the elastic section.

Figure 5 displays velocity streamlines for three solutions with Reynolds numbers of 10, 100 and 300. The contours are scaled the same for all three plots, with equal intervals between neighbouring streamlines. Thus the distance between adjacent streamlines is inversely proportional to the average fluid velocity in that region. The maximum collapse of the channel wall is about 83% in all three cases. In both the $Re = 100$ and 300 solutions the flow separates downstream of the point of maximum collapse, with detachment occurring earlier at higher Reynolds number. A series of downstream eddies is generated and one striking feature is the small length scale of these. Although increasing with increasing Reynolds number, the eddy size remains $O(1)$, not $O(Re)$ as seen in separating external flows behind bluff obstructions and predicted by Helmholz–Kirchoff free streamline models of laminar separation (see e.g. References 107 and 108). The results here seem to be in better agreement with the Prandtl–Batchelor description[108,109] which allows for finite eddy recirculation velocities. Such velocities in these solutions can be quite significant (Table I, $u_{\min}$) and secondary flow separation within the eddy, as predicted by the Prandtl–Batchelor[109] but not the Helmhotz–Kirchoff[107] model, then occurs as the fluid in the eddy flows against an adverse pressure gradient along the upper boundary. Confinement of the flow thus plays a significant role in the structure and scale of laminar flow separation, and adoption of theories developed in the context of unconfined flows (as in Reference 110) is likely to prove problematic.

Figure 6 illustrates the sensitivity of the large-scale flow structure to the degree of channel obstruction. All three solutions plotted have $Re = 100$, with the maximum membrane collapse varying between 78% and 98%. Note that although the eddy structures become more complex with increasing collapse, the lengths of the downstream eddies remain constant. This is true even though the flow separation point moves upstream as the fluid velocity increases and pressure decreases in the constricted region (see $u_{\max}$ and $P_{\min}$ entries in Table I). Thus, although varying slowly with Reynolds number (Figure 5), the eddy length scale appears to be insensitive to the degree of channel wall collapse. Eddy strength or total eddy circulation, on the other hand, does depend on the degree of collapse, increasing with increasing constriction. As recirculation eddy strengths increase, the flow between them takes on a remarkably square configuration, with regions of nearly horizontal flow connected by very narrow regions of significant vertical velocity (see Figures 5*c* and 6*c*).

The degree of membrane collapse in these solutions is determined by the membrane tension and internal fluid pressure, since both the external and exit pressures are held fixed. When horizontal variations in the internal pressure are small compared with the external pressure, membrane collapse occurs fairly symmetrically about the membrane midpoint. As the degree of channel collapse increases, however, the internal pressure in the fluid rises upstream of the obstruction. This introduces horizontal asymmetry in the membrane deformation, noticeable in Figure 6*c* and further illustrated in

Table I. Properties of the solutions presented in Figures 5–9 (as indicated in the left-hand column). The column definitions and entry values are discussed in the text

Figure		Re	P_e	T_0	y_{min}	y_{max}	u_{min}	u_{max}	v_{min}	v_{max}	P_{min}	P_{max}	P_t	ΔT_{min}	ΔT_{max}
5	*a*	10	5000	20000	0·17	1·00	0·00	9·00	−0·73	0·75	0·00	393	−4610	0·00	38·9
	b	100	5000	21000	0·18	1·00	−0·59	8·27	−0·72	0·63	−6·77	39·4	−4960	−0·07	3·52
	c	300	5000	20880	0·17	1·00	−2·27	7·99	−1·26	2·08	−8·14	24·5	−4980	−0·04	1·48
6	*a*	100	5000	22000	0·22	1·00	−0·43	6·56	−0·63	0·53	−3·82	24·2	−4980	−0·05	2·54
	b	100	5000	19000	0·08	1·00	−1·51	18·1	−1·10	1·37	−31·9	231	−4770	−0·16	10·9
	c	100	5000	10380	0·02	1·00	−4·12	62·5	−2·30	3·97	−298	3620	−1380	−0·51	56·3
7, 8*a*	(· · · · ·)	300	100	3000	0·90	1·00	0·00	1·61	−0·04	0·04	0·00	1·25	−98·9	0·00	0·12
	(– – – –)	300	100	1000	0·68	1·00	0·00	2·00	−0·15	0·12	0·00	1·51	−98·6	−0·00	0·19
	(— · —)	300	100	600	0·45	1·00	−0·21	2·92	−0·33	0·17	−0·96	2·70	−97·4	−0·01	0·36
	(———)	300	100	430	0·21	1·00	−1·69	6·33	−0·68	1·48	−5·51	14·6	−85·5	−0·03	1·07
7, 8*b*)	(· · · · ·)	300	10	300	0·90	1·00	0·00	1·60	−0·04	0·04	0·00	1·25	−8·93	0·00	0·12
	(– – – –)	300	10	60	0·45	1·00	−0·21	2·93	−0·32	0·18	−0·98	2·71	−7·43	−0·01	0·36
	(— · —)	300	10	25	0·22	1·00	−1·77	5·85	−0·74	1·55	−5·07	12·2	2·08	−0·02	0·86
	(———)	300	10	11	0·21	1·07	−1·96	5·85	−1·05	1·77	−5·48	12·4	2·19	−0·02	0·71
7, 8*c*	(· · · · ·)	300	0	30	1·00	1·10	0·00	1·50	−0·04	0·03	0·00	1·17	0·96	0·00	0·08
	(– – – –)	300	0	10	1·00	1·33	0·00	1·50	−0·11	0·07	0·00	1·14	0·91	0·00	0·04
	(— · —)	300	0	6	1·00	1·56	−0·07	1·50	−0·14	0·06	0·00	1·14	0·91	0·00	0·02
	(———)	300	0	4·4	1·00	1·78	−0·14	1·50	−0·17	0·05	0·00	1·14	0·92	−0·00	0·01
9	A	300	1	6·6	0·92	1·00	0·00	1·58	−0·03	0·03	0·00	1·24	0·05	0·00	0·12
	B	300	1	4·2	0·65	1·00	−0·04	2·06	−0·15	0·13	0·00	1·54	0·37	−0·00	0·20
	C	300	1	0·6	0·80	1·29	−0·03	1·66	−0·22	0·08	0·00	1·23	0·01	−0·00	0·08
	D	300	1	0·15	0·83	1·39	−0·07	1·61	−0·19	0·07	0·00	1·21	0·02	−0·00	0·07

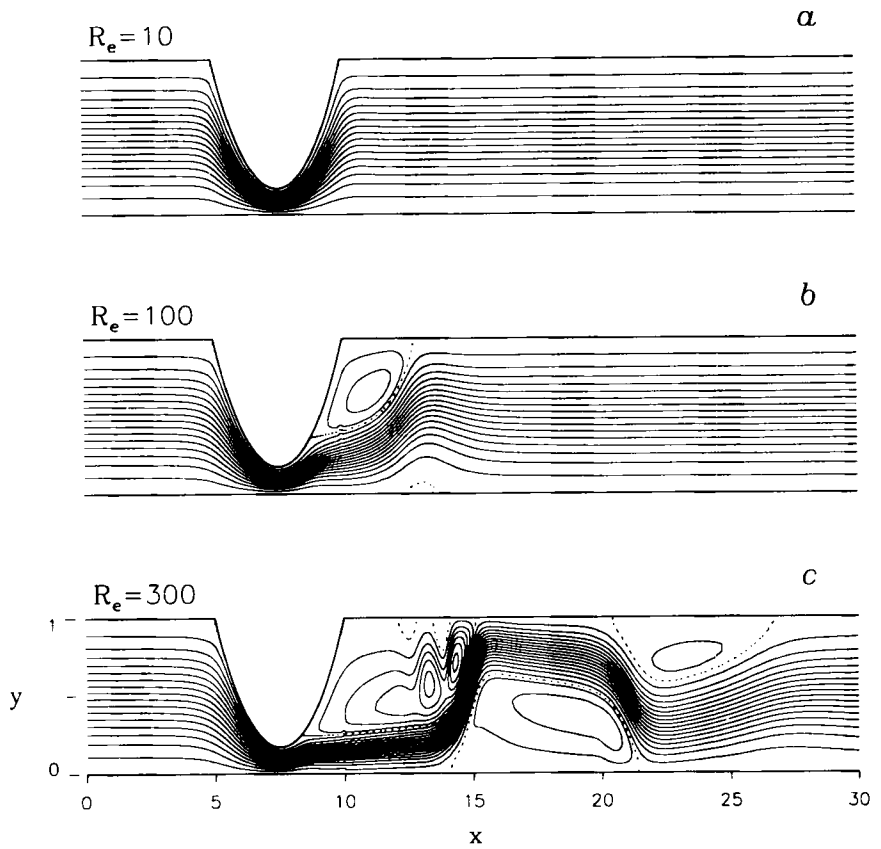

Figure 5. Velocity streamlines for three solutions with Reynolds numbers (*a*) 10, (*b*) 100 and (*c*) 300. Maximum channel collapse is about 83% in all three. Dashed lines indicate streamlines of value zero or one. The remaining streamlines are scaled the same for all three plots, with equal intervals between neighbouring values

Figure 7. In Figure 7 membrane height is plotted against horizontal position for various tensions at three different external pressures. In Figure 7*a* the external pressure is high, and despite the increase in the internal fluid pressure which accompanies collapse, the transmural pressure remains negative (Table I). Collapse thus occurs along the full length of the membrane for all values of tension shown. Figure 7*c* illustrates the opposite behaviour. Low external pressures and thus positive transmural pressures yield a bulging profile, with the degree of deformation increasing with decreasing tension. Between these extreme cases lie the solutions of Figure 7*b* in which the external pressure is moderate. For high values of T_0 the membrane is collapsed along its entire length. At lower tensions, however, the upstream pressure needed to drive the fluid through the constricted channel mounts and the transmural pressure becomes positive at the upstream end. The resulting wall shape is convex at the upstream end and concave at the downstream one. The sign of the curvature changes at the position where the transmural pressure equals zero.

For a given degree of collapse the shear stresses exerted by the fluid decrease with increasing Reynolds number (see ΔT entries in Table I for Figure 5), because the fluid viscosity decreases and the velocity profile through the constriction changes only little. Conversely, for a given Reynolds number and thus constant viscosity the maximum shear stresses exerted by the fluid on the membrane increase as the constriction narrows (Table I, Figure 6). Not only does the maximum change, but so too does the stress distribution along the membrane. Figure 8 plots the variation in membrane tension with position

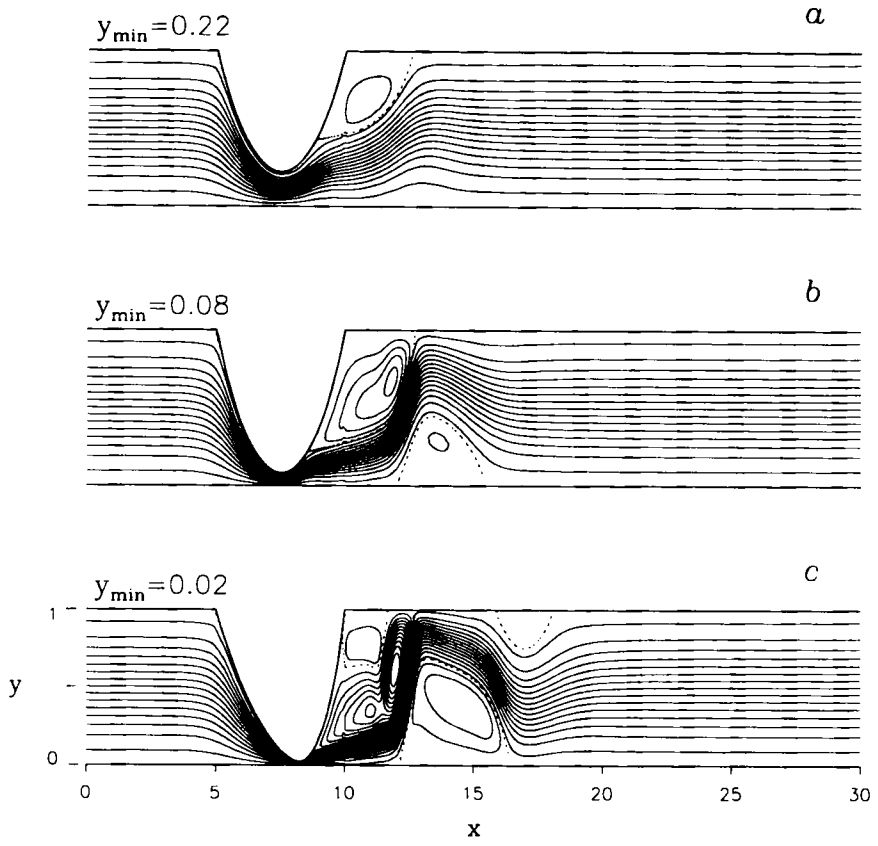

Figure 6. Velocity streamlines for three solutions with Reynolds number 100. Membrane tension and thus maximum collapse varies between them, with y_{min} taking values of (*a*) 0.22, (*b*) 0.08 and (*c*) 0.02. Dashed lines indicate streamlines of value zero or one. The remaining streamlines are scaled the same for all three plots, with equal intervals between neighbouring values

for those solutions of Figure 7. In general the elastic membrane is under greater tension at the upstream end than at the downstream one. However, the minimum value does not necessarily coincide with that at the right-hand side, T_0. When flow separation occurs, the minimum tension occurs just downstream of the maximum collapse, at the point of flow detachment (Figures 8*a* and 8*b*). Here the tangential velocity along the elastic boundary vanishes, as does the shear stress. Across the separation point the tangential velocity and shear stress change sign and the longitudinal membrane tension increases to either side. Similarly, in the bulging cases (Figure 8*c*) greatly reduced tangential flow velocities at the upstream end of the membrane result in very low values of shear stress there. In these cases the maximum tension can occur just before the right-hand membrane attachment point if the deformation is severe. Note, however, that in all these solutions the magnitudes of the variations in membrane tension are small, never exceeding 6·5% of T_0 in the solutions of Figures 5–8 (Table I).

Figure 9 illustrates a series of more extreme cases. In these the external pressure is of the same order as the internal pressure, so the transmural pressure along the membrane is very low. Membrane height is plotted against horizontal position for T_0 ranging between 6·6 and 0·15. For the higher values of T_0 the membrane deforms little (curve *A* in Figure 9) and rather substantial reductions in tension cause little change in position. Then quite suddenly, for a small decrease in the tension, the channel wall collapses to a position represented by curve *B*. Further reductions in T_0 yield solutions in which the upstream end of the elastic membrane bulges outwards and the downstream end inwards (curve *C*) as

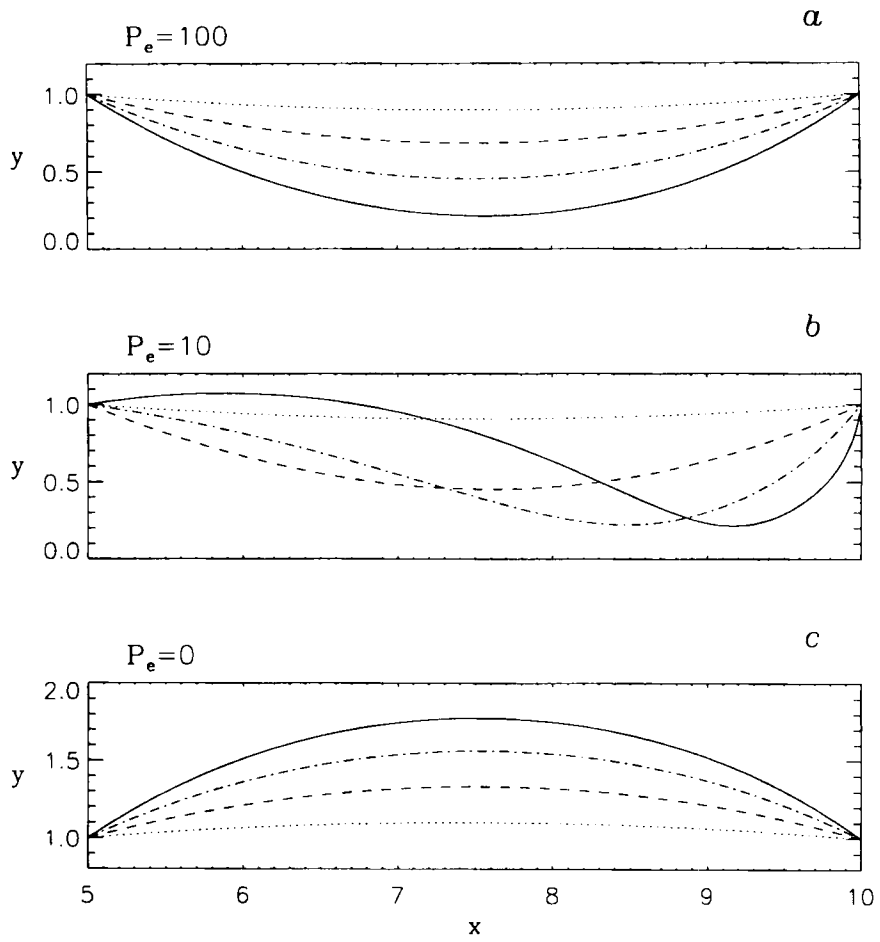

Figure 7. Membrane height y versus horizontal position x for various tensions (Table I) at external pressures of (*a*) 100, (*b*) 10 and (*c*) 0. At high external pressures the membrane is collapsed along its entire length, at moderate external pressures it can take on a partially collapsed, partially bulged configuration for low values of tension, and at low external pressures it expands outwards along its entire length

in the lowest-tension case of Figure 7*b*. At still lower tensions solutions are found in which the curvature changes sign twice (curve *D* in Figure 9). The membrane is partially collapsed at the upstream end, bulges outwards in the middle and is partially collapsed again at the downstream end. Such solutions show substantial horizontal variations in membrane tension. The tension has its maximum value at the upstream end, is fairly constant in the middle and reaches a minimum just before the right-hand attachment point. The relative magnitudes of these variations are large, approaching 50% of T_0, so that the overall membrane shape is likely to be significantly different from that which would be obtained with a constant tension model.

5. CONCLUSION

We have successfully solved the non-linear equations governing fluid motion in a channel with an elastic boundary. We have done so assuming that the motions are time-independent and have found solutions which simultaneously satisfy the steady Navier–Stokes and elastic membrane equations.

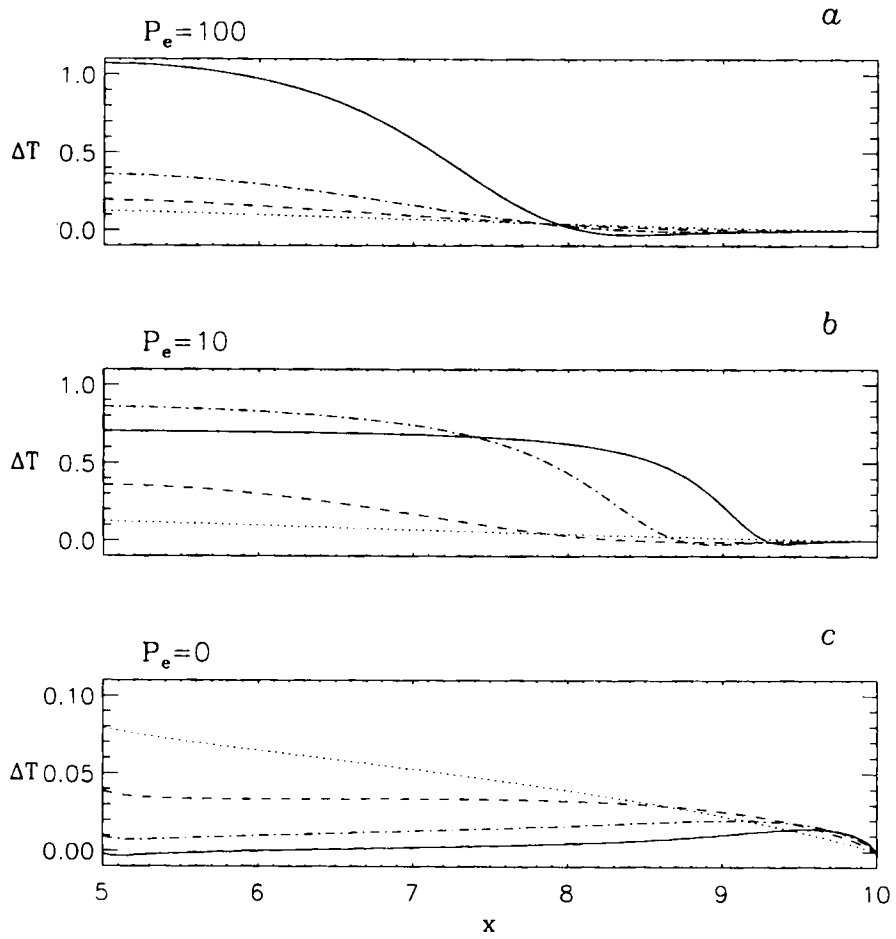

Figure 8. Variations in membrane tension $\Delta T = T - T_0$ with horizontal position x for those membrane configurations plotted in Figure 7. These variations arise owing to shear stresses exerted by the fluid motions on the membrane. Note that for the most deformed cases (solid curves) the minimum tension does not occur at the right-hand attachment point

Numerical convergence remains quadratic when care is taken in constructing the grid. Particular sensitivity was noticed at the right-hand side of the elastic section when the element size there, owing to deformation of the elastic boundary, did not match that of the regular non-deformed grid downstream. In some cases substantial gains in convergence rates were obtained by repositioning the spine origin and compressing the downstream grid so that changes in element size were gradual. With the present spine configuration, however, limits are reached when the slope of the downstream end of the elastic membrane becomes nearly vertical. Such limits are readily overcome by adapting the methods used here to the particular membrane shape of interest. Incorporation of multiple spine origins would prove useful for cases in which the elastic membrane is sucked downstream of its right-hand attachment point. The generalizability of the spine method to such complex boundary geometries makes it particularly appealing for further work on this problem and related moving boundary problems in general.

The steady solutions we obtained and discussed in this paper display complex flow structure and boundary shapes, with the large-scale structure of the flows being significantly influenced by the geometry of the boundary and the confinement of the flow. Some of these solutions are likely to be

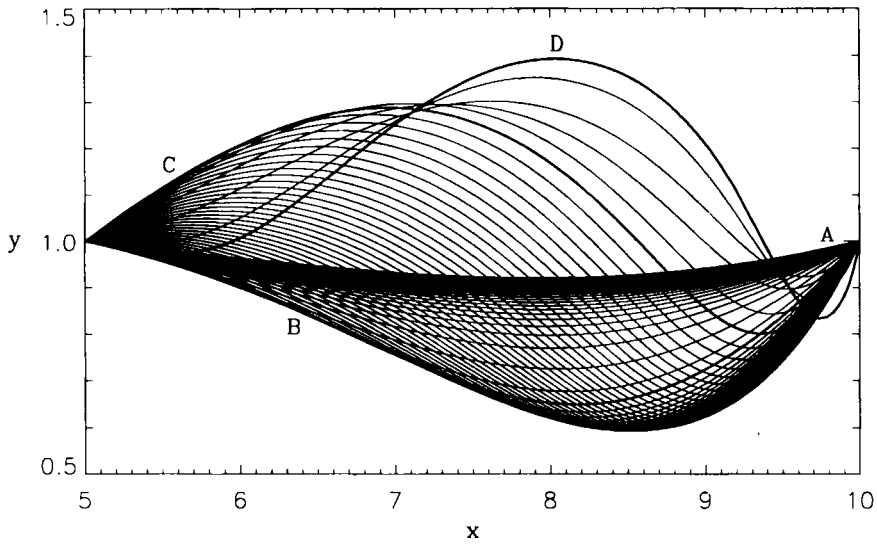

Figure 9. Membrane height y versus horizontal position x for solutions of low transmural pressure and very low membrane tension. The sequence proceeds from A to D with T_0 ranging from 6.6 to 0.15 in steps of 0.1 (except for the last step which has an increment of 0.05). The external pressure is the same in all cases. Note that four quite distinct regimes of membrane shape are accessed by the solutions

unstable and would be time-dependent if so allowed. This raises the question of how readily the method described in this paper can be incorporated into a time-dependent code. An Adams–Bashforth predictor, trapezoid rule corrector scheme (see e.g. Reference 111) should be readily adaptable to this problem as it has been to viscous free surface flows.[75] One must in turn question the validity of the simple membrane model used here in a time-dependent calculation. In this model we held T_0 constant at the right-hand side of the membrane. In doing this, we implicitly assume an initial stress configuration (prestretch) of the membrane consistent with the subsequent loading, displacement and tension of the solution. This poses no problem for the steady solution, but in a time-dependent analysis such implied initial conditions would change with changes in the membrane deformation and this is unsatisfactory. A more physically appealing description would be to treat the membrane as a two-dimensional beam, or in three dimensions as a shell, and solve the non-linear equations of elasticity for Lagrangian displacements of the boundary. These equations could replace the two membrane equations in the current formulation and be incorporated into the finite element spine algorithm by expressing the nodal co-ordinates of the grid in terms of membrane displacements, allowing for both vertical and lateral deformation of the elements in response to that of the elastic boundary. Such an effort is likely to yield a rich reward in the understanding of the physical breakdown of steady flow in this coupled fluid elastic problem.

ACKNOWLEDGEMENTS

Special thanks are given to P. Charbonneau, J. Klemp, T. Lowe, K. MacGregor, T. Pedley, M. Savage, J. Summers and R. Rotunno. This work was supported in part by the Science and Engineering Research Council through grant GR/F69925. Computations were carried out on a Silicon Graphics Challenge XL at the Leeds University Computing Service Computationally Intensive Facility.

REFERENCES

1. A. H. Shapiro, 'Physiologic and medical aspects of flow in collapsible tubes', in V. J. Modi (ed.), *Proc. Sixth Can. Congr. on Applied Mechanics*, Vancouver, 1977, p. 883.
2. T. J. Pedley, *The Fluid Mechanics of Large Blood Vessels*, Cambridge University Press, Cambridge, 1980.
3. R. D. Kamm and T. J. Pedley, 'Flow in collapsible tubes: a brief review', *J. Biomech. Eng.*, **111**, 177 (1989).
4. R. Skalak, N. Özkaya and T. C. Skalak, 'Biofluid mechanics', *Ann. Rev. Fluid Mech.*, **21**, 167 (1989).
5. C. G. Caro, J. M. Fitz-Gerald and R. C. Schroter, 'Atheroma and arterial wall shear: observation, correlation and proposal of a shear dependent mass transfer mechanism for atherogenesis', *Proc. R. Soc. Lond. B*, **177**, 109 (1971).
6. D. N. Ku, D. P. Giddens, C. K. Zarins and S. Glagov, 'Pulsatile flow and atherosclerosis in the human carotid bifurcation: positive correlation between plague location and low and oscillatory shear stress', *Arteriosclerosis*, **5**, 293 (1985).
7. J. B. Grotberg and S. H. Davis, 'Fluid-dynamic flapping of a collapsible channel: sound generation and flow limitation', *J. Biomech.*, **13**, 219 (1980).
8. N. Gavriely, Y. Palti, G. Alroy and J. B. Grotberg, 'Measurement and theory of wheezing breath sounds', *J. Appl. Physiol.: Respirat. Environ. Exercise Physiol.*, **57**, 481 (1984).
9. A. Ur and M. Gordon, 'Origin of Korotkoff sounds', *Am. J. Physiol.*, **218**, 524 (1970).
10. W. A. Conrad, D. M. McQueen and E. L. Yellin, 'Steady pressure flow relations in compressed arteries: possible origin of Korotkoff sounds', *Med. Biol. Eng. Comput.*, **18**, 419 (1980).
11. A. G. Hudetz, R. J. Roman and D. R. Harder, 'Spontaneous flow oscillations in the cerebral cortex during acute changes in mean arterial pressure', *J. Cereb. Blood Flow Metabol.*, **12**, 491 (1992).
12. W. V. Martinez Jr., personal communication, 1994.
13. F. P. Knowlton and E. H. Starling, 'The influence of variations in temperature and blood pressure on the performance of the isolated mammalian heart', *J. Physiol.*, **44**, 206 (1912).
14. S. W. Patterson and E. H. Starling, 'On the mechanical factors which determine the output of the ventricles', *J. Physiol.*, **48**, 357 (1914).
15. W. A. Conrad, 'Pressure–flow relationships in collapsible tubes', *IEEE Trans. Biomed. Eng.*, **BME-16**, 284 (1969).
16. A. I. Katz, Y. Chen and A. H. Moreno, 'Flow through a collapsible tube', *Biophys. J.*, **9**, 1261 (1969).
17. R. W. Brower and C. Scholten, 'Experimental evidence on the mechanism for the instability of flow in collapsible vessels', *Med. Biol. Eng.*, **13**, 839 (1975).
18. D. J. Griffiths, 'Oscillations in the outflow from a collapsible tube', *Med. Biol. Eng. Comput.*, **15**, 357 (1977).
19. C. K. Lyon, J. B. Scott, D. K. Anderson and C. Y. Wang, 'Flow through collapsible tubes at high Reynolds numbers', *Circulat. Res.* **49**, 988 (1981).
20. C. D. Bertram, 'Two modes of instability in a thick-walled collapsible tube conveying a flow', *J. Biomech.*, **15**, 223 (1982).
21. C. D. Bertram, 'Unstable equilibrium behavior in collapsible tubes', *J. Biomech.*, **19**, 61 (1986).
22. C. D. Bertram, 'The effects of wall thickness, axial strain and end proximity on the pressure–area relation of collapsible tubes', *J. Biomech.*, **20**, 863 (1987).
23. C. D. Bertram, C. J. Raymond and T. J. Pedley, 'Mapping of instabilities during flow through collapsed tubes of differing length', *J. Fluids Struct.*, **4**, 125 (1990).
24. C. D. Bertram, C. J. Raymond and T. J. Pedley, 'Application of nonlinear dynamics concepts to the analysis of self-excited oscillations of a collapsible tube conveying fluid', *J. Fluids Struct.*, **5**, 391 (1991).
25. G. C. Oates, 'Fluid flow in soft-walled tubes: I. Steady flow', *Med. Biol. Eng.*, **13**, 773 (1975).
26. A. H. Shapiro, 'Steady flow in collapsible tubes', *ASME J. Biomech. Eng.*, **99**, 126 (1977).
27. D. W. Schoendorfer and A. H. Shapiro, 'The collapsible tube as a prosthetic vocal source', *Proc. San Diego Biomed. Symp.*, **16**, 349 (1977).
28. W. A. Conrad, M. L. Cohen and D. M. McQueen, 'Note on the oscillations of collapsible tubes', *Med. Biol. Eng. Comput.*, **16**, 211 (1978).
29. C. D. Bertram and T. J. Pedley, 'A mathematical model of unsteady collapsible tube behavior', *J. Biomech.*, **15**, 39 (1982).
30. S. V. Dawson and E. A. Elliott, 'Wave-speed limitation on expiratory flow—a unifying concept', *J. Appl. Physiol.: Respirat. Environ. Exercise Physiol.*, **43**, 498 (1977).
31. I. Kececioglu, M. E. McClurken, R. D. Kamm and A. H. Shapiro, 'Steady, supercritical flow in collapsible tubes. Part 1. Experimental observations', *J. Fluid Mech.*, **109**, 367 (1981).
32. M. E. McClurken, I. Kececioglu, R. D. Kamm and A. H. Shapiro, 'Steady, supercritical flow in collapsible tubes. Part 1. Theoretical studies', *J. Fluid Mech.*, **109**, 391 (1981).
33. S. J. Cowley, 'Elastic jumps on fluid-filled elastic tubes', *J. Fluid Mech.*, **116**, 459 (1982).
34. M. Shimizu and Y. Tanida, 'On the mechanism of Korotkoff sound generation at diastole', *J. Fluid Mech.*, **127**, 315 (1983).
35. M. Shimizu, 'Characteristics of pressure-wave propagation in a compliant tube with a fully collapsed segment', *J. Fluid Mech.*, **158**, 113 (1985).
36. M. Shimizu, 'Characteristics of shock-wave propagating through a partially-collapsed rubber tube', *Phys. Med. Biol.*, **33**, Suppl. I, 260 (1988).
37. C. Cancelli and T. J. Pedley, 'A separated-flow model for collapsible-tube oscillations', *J. Fluid Mech.*, **157**, 375 (1985).
38. J. W. Reyn, 'Multiple solutions and flow limitation for steady flow through a collapsible tube held open at the ends', *J. Fluid Mech.*, **174**, 467 (1987).
39. O. E. Jensen and T. J. Pedley, 'The existence of steady flow in a collapsed tube', *J. Fluid Mech.*, **206**, 339 (1989).
40. O. E. Jensen, 'Instabilities of flow in a collapsed tube', *J. Fluid Mech.*, **220**, 623 (1990).

41. T. J. Pedley, 'Longitudinal tension variation in collapsible channels: a new mechanism for the breakdown of steady flow', *ASME J. Biomech. Eng.*, **114**, 60 (1992).
42. T. W. Lowe and T. J. Pedley, 'Finite element solution of Stokes flow in a channel with a collapsible segment', in J. M. Crolet and R. Ohayon (eds.), *Computational Methods for Fluid Structure Interaction*, Longmans, London, 1994, p. 220.
43. X. Y. Luo and T. J. Pedley, 'A numerical simulation of steady flow in a 2-D collapsible channel', *J. Fluids Struct.*, submitted.
44. K. D. Stephanoff, T. J. Pedley, C. J. Lawrence and T. W. Secomb, 'Fluid flow along a channel with an asymmetric oscillating constriction', *Nature*, **305**, 692 (1983).
45. T. J. Pedley and K. D. Stephanoff, 'Flow along a channel with a time-dependent indentation in one wall: the generation of vorticity waves', *J. Fluid Mech.*, **160**, 337 (1985).
46. M. E. Ralph and T. J. Pedley, 'Flow in a channel with a moving indentation', *J. Fluid Mech.*, **190**, 87 (1988).
47. M. E. Ralph and T. J. Pedley, 'Viscous and inviscid flows in a channel with a moving indentation', *J. Fluid Mech.*, **209**, 543 (1989).
48. L. K. Shayo and C. H. Ellen, 'The stability of finite length circular cross-section pipes conveying inviscid fluid', *J. Sound Vibr.*, **37**, 535 (1974).
49. A. D. Garrad and P. W. Carpenter, 'A theoretical investigation of flow-induced instabilities in compliant coatings', *J. Sound Vibr.*, **85**, 483 (1982).
50. O. R. Tutty, 'High-Reynolds-number viscous flow in collapsible tubes', *J. Fluid Mech.*, **146**, 451 (1984).
51. J. B. Grotberg and E. L. Reiss, 'Subsonic flapping flutter', *J. Sound Vibr.*, **92**, 349 (1984).
52. J. B. Grotberg and T. R. Shee, 'Compressible-flow channel flutter', *J. Fluid Mech.*, **159**, 175 (1985).
53. M. P. Païdoussis, A. K. Misra and S. P. Chan, 'Dynamics and stability of coaxial cylindrical shells conveying viscous fluid', *J. Appl. Mech.*, **52**, 389 (1985).
54. P. W. Carpenter and A. D. Garrad, 'The hydrodynamic stability of flow over Kramer-type compliant surfaces. Part 1. Tollmien–Schlichting instabilities', *J. Fluid Mech.*, **155**, 465 (1985).
55. P. W. Carpenter and A. D. Garrad, 'The hydrodynamic stability of flow over Kramer-type compliant surfaces. Part 2. Flow-induced surface instabilities', *J. Fluid Mech.*, **170**, 199 (1986).
56. M. P. Païdoussis and A. D. Mateescu, 'Dynamics of cylindrical shells containing fluid flows with a developing boundary layer', *AIAA J.*, **25**, 857 (1987).
57. N. Kondo, N. Tosaka and T. Nishimura, 'Numerical simulation for coupled system of viscous flow and elastic shell', in C. Taylor, W. G. Habashi and M. M. Hafez (eds.), *Numerical Methods in Laminar and Turbulent Flow*, Vol. 5, Part 2, Pineridge, Swansea, 1987, p. 1798.
58. O. A. Likhachev, 'Investigation of organized structures in the near-wall turbulent boundary layer zone on a partially deformable surface', *J. Appl. Mech. Tech. Phys.*, **29**, 661 (1988).
59. V. Shankar and H. Ide, 'Aeroelastic computations of flexible configurations', *Comput. Struct.*, **30**, 15 (1988).
60. L. L. Broderick and J. W. Leonard, 'Selective review of boundary element modelling for the interaction of deformable structure with water waves', *Eng. Struct.*, **12**, 269 (1990).
61. M. Pierucci and P. G. Morales, 'Effect of finite thickness flexible boundary upon the stability of a Poiseuille flow', *Trans. ASME J. Appl. Mech.*, **57**, 1056 (1990).
62. V. F. Poterasu, 'Coupled vibrations of a cavity filled with a pulsating fluid in elastic infinite media by the boundary element method', *Comput. Methods Appl. Mech. Eng.*, **106**, 285 (1993).
63. C. Farhat and T. Y. Lin, 'Structure-attached corotational fluid grid for transient aeroelastic computations', *AIAA J.*, **31**, 597 (1993).
64. R. E. Nickell, R. I. Tanner and B. Caswell, 'The solution of viscous incompressible jet and free-surface flows using finite-element methods', *J. Fluid Mech.*, **65**, 189 (1974).
65. F. M. Orr and L. E. Scriven, 'Rimming flow: numerical simulation of steady, viscous, free-surface flow with surface tension', *J. Fluid Mech.*, **84**, 145 (1978).
66. K. R. Reddy and R. I. Tanner, 'Finite element solution of viscous jet flows with surface tension', *Comput. Fluids*, **6**, 83 (1978).
67. W. J. Silliman and L. E. Scriven, 'Separating flow near a static contact line: slip at a wall and shape of a free surface', *J. Comput. Phys.*, **34**, 287 (1980).
68. C. S. Frederiksen and A. M. Watts, 'Finite-element method for time-dependent incompressible free surface flow', *J. Comput. Phys.*, **39**, 282 (1981).
69. W. J. Silliman, 'Viscous film flows with contact lines', *Ph.D. Thesis*, University of Minnesota, 1979.
70. K. J. Ruschak, 'A method for incorporating free boundaries with surface tension in finite element fluid-flow simulators', *Int. j. numer. methods eng.*, **15**, 639 (1980).
71. H. Saito and L. E. Scriven, 'Study of coating flow by the finite element method', *J. Comput. Phys.*, **42**, 53 (1981).
72. S. F. Kistler, 'The fluid mechanics of curtain coating and related viscous free suface flows with contact lines', *Ph.D. Thesis*, University of Minnesota, 1983.
73. S. F. Kistler and L. E. Scriven, 'Coating flows', in J. R. A. Pearson and S. M. Richardson (eds.), *Computational Analysis of Polymer Processing*, Applied Science Publishers, London, 1983, p. 243.
74. S. F. Kistler and L. E. Scriven, 'Coating flow theory by finite element and asymptotic analysis of the Navier–Stokes system', *Int. j. numer. methods fluids*, **4**, 207 (1984).
75. H. S. Kheshgi and L. E. Scriven, 'Penalty finite element analysis of unsteady free surface flows', in R. H. Gallagher, J. T. Oden, O. C. Zienkiewicz, T. Kawai and M. Kawahara (eds.), *Finite Elements in Fluids*, Vol. 5, Wiley, New York, 1984, p. 393.

76. H. M. Thompson, 'A theoretical investigation of roll coating phenomena', *Ph.D. Thesis*, University of Leeds, 1992.
77. J. L. Summers, personal communication, 1993.
78. F. H. Harlow and A. A. Amsden, 'A numerical fluid dynamics calculation method for all flow speeds', *J. Comput. Phys.*, **8**, 197 (1971).
79. C. W. Hirt, A. A. Amsden and J. L. Cook, 'An arbitrary Lagrangian–Eulerian computing method for all flow speeds', *J. Comput. Phys.*, **14**, 227 (1974).
80. W. E. Pracht, 'Calculating three-dimensional fluid flows at all speeds with an Eulerian–Lagrangian computing mesh', *J. Comput. Phys.*, **17**, 132 (1975).
81. R. K.-C. Chan, 'A generalized arbitrary Lagrangian–Eulerian method for incompressible flows with sharp interfaces', *J. Comput. Phys.*, **17**, 311 (1975).
82. Y. Mizuta, 'Generalized boundary conditions on the basis of a deformable-cell method: free surfaces, density interfaces and open boundaries', *Comput. Fluids*, **19**, 377 (1991).
83. B. J. Daly, 'A technique for including surface tension effects in hydrodynamic calculations', *J. Comput. Phys.*, **4**, 97 (1969).
84. R. K.-C. Chan and R. L. Street, 'A computer study of finite amplitude water waves', *J. Comput. Phys.*, **6**, 68 (1970).
85. J. A. Viecelli, 'A computing method for incompressible flows bounded by moving walls', *J. Comput. Phys.*, **8**, 119 (1971).
86. C. W. Hirt and B. D. Nichols, 'Volume of fluid (VOF) method for the dynamics of free boundaries', *J. Comput. Phys.*, **39**, 201 (1981).
87. C. A. Brebbia, *The Boundary Element Method for Engineers*, Pentech, London, 1978.
88. R. I. Tanner, 'Extrudate swell', in J. R. A. Pearson and S. M. Richardson (eds.), *Computational Analysis of Polymer Processing*, Applied Science Publishers, London, 1983, p. 63.
89. D. B. Ingham, 'Viscous free surface flows', in L. C. Wrobel and C. A. Brebbia (eds.), *Computational Methods for Free and Moving Boundary Problems in Heat and Fluid Flow*, Computational Mechanics Publications, Southampton, 1993, p. 117.
90. B. Ramaswamy and M. Kawahara, 'Arbitrary Lagrangian–Eulerian finite element method for unsteady, convective, incompressible viscous free surface fluid flow', *Int. j. numer. methods fluids*, **7**, 1053 (1987).
91. J. F. Thompson and Z. U. A. Warsi, 'Boundary-fitted coordinate systems for numerical solution of partial differential equations–a review', *J. Comput. Phys.*, **47**, 1 (1982).
92. G. Ryskin and L. G. Leal, 'Orthogonal mapping', *J. Comput. Phys.*, **50**, 71 (1983).
93. G. Ryskin and L. G. Leal, 'Numerical solution of free-boundary problems in fluid mechanics. Part 1. The finite-difference technique', *J. Fluid Mech.*, **148**, 1 (1984).
94. G. Ryskin and L. G. Leal, 'Numerical solution of free-boundary problems in fluid mechanics. Part 2. Buoyancy-driven motion of a gas bubble through a quiescent liquid', *J. Fluid Mech.*, **148**, 19 (1984).
95. G. Ryskin and L. G. Leal, 'Numerical solution of free-boundary problems in fluid mechanics. Part 3. Bubble deformation in an axisymmetric straining flow', *J. Fluid Mech.*, **148**, 37 (1984).
96. C. S. Peskin, 'Flow patterns around heart valves: a numerical method', *J. Comput. Phys.*, **10**, 252 (1972).
97. C. S. Peskin, 'Numerical analysis of blood flow in the heart', *J. Comput. Phys.*, **25**, 220 (1977).
98. O. C. Zienkiewicz, *The Finite Element Method in Engineering Science*, McGraw-Hill, London, 1977.
99. T. J. Chung, *Finite Element Analysis of Fluid Dynamics*, McGraw-Hill, New York, 1978.
100. P. S. Huyakorn, C. Taylor, R. L. Lee and P. M. Gresho, 'A comparison of various mixed interpolation finite elements in the velocity pressure formulation of the Navier–Stokes equations', *Comput. Fluids*, **6**, 25 (1978).
101. G. R. Cowper, 'Gaussian quadrature formulas for triangles', *Int. j. numer. methods eng.*, **7**, 405 (1973).
102. R. A. Brown, L. E. Scriven and W. J. Silliman, 'Computer-aided analysis of nonlinear problems in transport phenomena', in P. J. Holmes (ed.), *New Approaches to Nonlinear Problems in Dynamics*, SIAM, Philadelphia, 1980, p. 289.
103. B. M. Irons, 'A frontal solution program for finite element analysis', *Int. j. numer. methods eng.*, **2**, 5 (1970).
104. P. Hood, 'Frontal solution program for unsymmetric matrices', *Int. j. numer. methods eng.*, **10**, 379 (1976).
105. P. Hood, 'Note on frontal solution program for unsymmetric matrices', *Int. j. numer. methods eng.*, **11**, 1055 (1977).
106. Leeds Coating-Flow Group, personal communication, 1993.
107. F. T. Smith, 'Laminar flow of an incompressible fluid past a bluff body: the separation, reattachment, eddy properties and drag', *J. Fluid Mech.*, **92**, 171 (1979).
108. F. T. Smith, 'Steady and unsteady boundary-layer separation', *Ann. Rev. Fluid Mech.*, **18**, 197 (1986).
109. G. K. Batchelor, 'A proposal concerning laminar wakes behind bluff bodies at large Reynolds number', *J. Fluid Mech.*, **1**, 388 (1956).
110. F. T. Smith, 'The separating flow through a severely constricted symmetric tube', *J. Fluid Mech.*, **90**, 725 (1979).
111. P. M. Gresho, R. L. Lee and R. L. Sani, 'On the time-dependent solution of the incompressible Navier–Stokes equations in two and three dimensions', in C. Taylor and K. Morgan (eds.), *Recent Advances in Numerical Methods in Fluids*, Vol. 1, Pineridge, Swansea, 1979, p. 27.